Montanuniversität Leoben

Ductile Mo-Re Thin Films for Flexible Displays

Filipe Hauser

The following thesis was conducted in cooperation with PLANSEE SE, within the Competence Headquartes Project E^2-Sputtertech, with financial support from the Österreichische Forschungsförderungsgesellschaft at the Chair of Functional Materials and Materials Systems, Montanuniversität Leoben, Austria.

Leoben, September 2016

Affidavit:

I declare in lieu of oath, that I wrote this thesis and performed the associated research myself, using no other than the declared sources.

Leoben, September 2016 Filipe Hauser

Acknowledgments

My sincere gratitude goes to Prof. Dr. Christian Mitterer for giving me the opportunity to carry out and write this thesis at the Chair of Functional Materials and Materials Systems as well as for the confidence he has placed in me.

Further, I am hugely grateful to my supervisor Dipl.-Ing. Tanja Jörg for her words of advice, her great expertise and her patience during the research and writing of this thesis. Without her guidance, this work would not have been accomplished.

I also want to express my gratitude to Dr. Robert Franz for his assistance and help during the process of this thesis.

I would like to thank Dr. Megan Cordill and Dr. Oleksandr Glushko for their outright support and assistance during the measurements at their facilities at the Erich Schmidt Institute of Material Science.

I am very thankful to Dr. Jörg Winkler and Dr. Harald Köstenbauer from PLANSEE SE for the collaboration and for providing me the targets for the depositions.

I would like extend my sincere thanks to all of those who have helped me with the sample preparation and the analysis, especially Veli, who was a great helping hand and always had an open ear for me. Many thanks also to Hilde, who managed everything quickly and unbureaucratically.

Further, I would like to thank my friends and colleagues of the "Thin Film Group" for their support and encouraging words, in particular those who endured my little but always friendly tricks and jokes.

Above all, I am deeply grateful to my parents. Thank you for your support, your love and your encouragement in every aspect over all the years.

Contents

1 Introduction **1**

2 Theoretical aspects **2**

2.1 Physical vapor deposition 2

2.2 Magnetron sputtering 3

2.3 Nucleation and film growth 5

2.4 Microstructure 6

2.5 Mechanical properties 7

2.5.1 Metal thin films on compliant substrates 7

2.5.2 Deformation behavior of ductile films 8

2.5.3 Deformation behavior of brittle films 9

2.5.4 Fragmentation testing 10

2.5.5 Performance enhancement of brittle films 11

2.6 Electrical properties 12

2.6.1 Metal thin films compared to bulk material 12

2.6.2 *In situ* 4 Point Probe measurement 12

2.7 The molybdenum-rhenium system 15

3 Experimental methods **17**

3.1 Sputter deposition 17

3.2 Thin film characterization 18

3.2.1 Film thickness 18

3.2.2 Chemical composition 18

3.2.3 Microstructure 18

3.2.4 Sheet resistivity 19

3.2.5 Residual stress 19

3.3 Heat treatment 20

3.4 Tensile straining 20

3.4.1 Electro-mechanical testing 20

3.4.2 Fragmentation tests 22

4 Results and discussion **23**

4.1 Chemical composition 23

4.2 Microstructure 23

4.3 Annealing tests 25

4.4 Sheet resistivity 25

4.5 Residual stress measurements 26
4.6 Electro-mechanical behavior 28
4.6.1 *In situ* 4PP tensile tests 28
4.6.2 Crack density measurements 31

5 Summary and conclusions **34**

1 Introduction

In the upcoming years, flexible electronics such as smart textiles, electronic skin and especially bendable displays are expected to be launched on a large-scale market. Even though considerable progress has been made in recent years, several challenges still lay ahead. Besides low production costs, these multicomponent electronics need to be robust and reliable regarding their electro-mechanical properties in order to withstand mechanical loads without electrically failing. One of those components are metal film conductors, which are used as interconnects between the electronic switching elements in displays, e.g. thin film transistors (TFTs) [1, 2].

The interplay of compliant polymer substrates and conducting metal thin films has become an important key factor for the electrical and mechanical stability of flexible electronics during stretching, compressing and bending [3]. Several thin metal layers have been of great scientific and industrial interest for their usage in flexible electronics. In the established display technologies on rigid substrates, molybdenum thin films have proven to be a suitable material for gate and source/drain interconnects as well as data bus-lines in TFTs due to their low electrical resistance in combination with a high thermal and chemical stability. However, the usage of Mo for flexible displays is limited because of its brittle behavior during mechanical loading [4].

Since the 1950s Mo-Re alloys are known to exhibit extraordinary workability even at low temperatures, which is attributed to a so-called "Re-effect" [5, 6]. The effect is related to an enhancement of the dislocation mobility as well as a reduced embrittlement by impurities in Mo-Re alloys. Even though the Mo-Re alloys were designated for applications in the aerospace industry at that time, these remarkable alloys could also be suitable as metal thin films for flexible display applications nowadays.

Therefore, a strategy to improve the fracture behavior of the brittle Mo thin films by alloying them with Re is explored within this work. Its focus lies in the investigation of the deformation behavior of these films when strained in tension and the Re content is varied. Thus, Mo films with different Re concentrations have been deposited via magnetron sputtering on polyimide substrates. A general analysis of the relevant properties of the as deposited Mo-Re thin films was conducted by performing energy dispersive X-ray spectroscopy, X-ray diffraction spectroscopy as well as sheet resistivity and residual stress measurements. Finally, tensile tests with *in situ* electrical resistance measurements were conducted to determine the electrical response in relation to the applied strain. Furthermore, optical observation during tensile straining gave a deeper insight on the fracture behavior of the deposited Mo-Re films.

2 Theoretical aspects

2.1 Physical vapor deposition

One major group of thin film deposition techniques can be categorized as physical vapor deposition (PVD) processes. They are characterized by physically transferring a liquid or solid material into a vapor. The formed vapor is transported to a substrate surface, where its condensation is followed by nucleation and film growth. There are several physical processes used to vaporize a material classifying the different PVD methods such as thermal evaporation, cathodic arc evaporation, ion plating or sputtering, to name a few. With PVD it is possible to deposit thin films of variable thickness and almost unrestricted composition in a cost-saving way [7]. In microelectronics this has led to a major use of PVD, e.g. in the fabrication of conductive paths for display technologies [8]. Some further fields of application are the automotive, aerospace and tool industry, where hard coatings as well as corrosion-, heat- and wear-resistant coatings are essential [7].

In sputter deposition processes, atoms are physically evaporated from a solid target by bombardement with gaseous ions (e.g. Ar^+). As schematically shown in Fig. 2.1, a gas discharge providing the bombarding ions is generated by applying a high voltage between two electrodes in a low gas pressure environment, causing the electrons to move rapidly from the cathode to the anode in the electric field. Due to their low mass, the electrons reach a high kinetic energy, which results in excitation and ionization of the heavy gas atoms during collisions with the moving electrons. These excitation processes create a bright glowing plasma, which was first observed by Grove in 1852 [9].

As a consequence to their positive charge, the ions are accelerated in the electric field towards the cathode surface, called target. The following high energy impact leads to

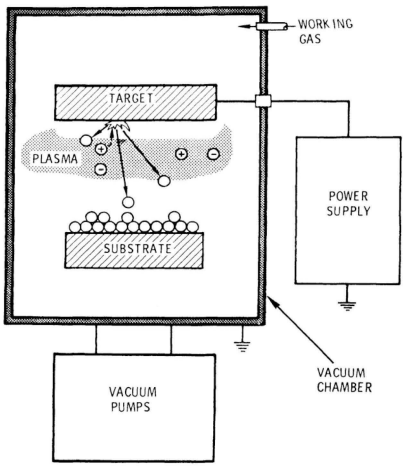

Fig. 2.1: Schematic setup of a vaccum chamber for sputter deposition. Note that the target is used as a cathode [9].

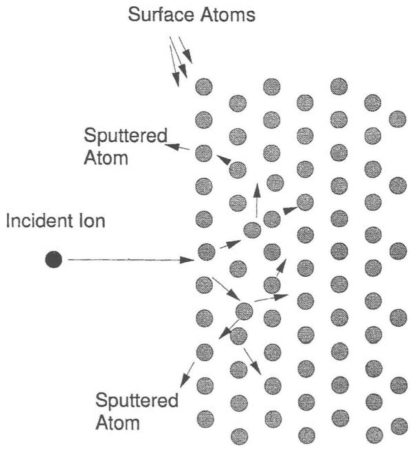

Fig. 2.2: The collision cascade causes substrate atoms to be ejected. Further, particles like secondary electrons and repelled ions or neutrals can be emitted (not shown here) [8].

a collision cascade in the target material and, as a result, atoms are ejected from the surface. This fundamental process is known as sputtering. A schematic illustration of the colliding processes in the near-surface region of the target is given in Fig. 2.2. The performance of the sputtering behavior for a certain target element is described by the sputter yield, which is defined as the ratio of the number of emitted atoms to the number of incident ions. The main effects on the sputter yield are the atomic mass ratio between the incoming ion and the atom in the target as well as the surface binding energy of the target material [10].

In conventional diode glow discharge arrangements as described so far, the achievable sputter rate and, hence, deposition rate is rather low due to the low plasma density near the target. Higher plasma densities can be reached in so-called magnetron configurations, which enable cost-effective deposition processes due to sufficiently high deposition rates [10].

2.2 Magnetron sputtering

Magnetron sputtering is established as the dominating method in the PVD industry with an estimated usage of approximately 95 % of all sputtering applications. The efficiency of the sputtering process is considerably amplified by installing a magnetic field via permanent magnets in the vicinity of the cathode or target. By arranging the magnets as it is shown in Fig. 2.3, the magnetic field lines form an ideally closed loop on top of the target. The huge advantage of the magnet arrangement comes from an effect known as the $E \times B$ drift. Due to the Lorentz force, charged particles in the plasma are forced to move in trajectories perpendicular to the magnetic field and the electric field lines, while the mass dependence of the Lorentz force leads to the fact that only electrons are subjected to the

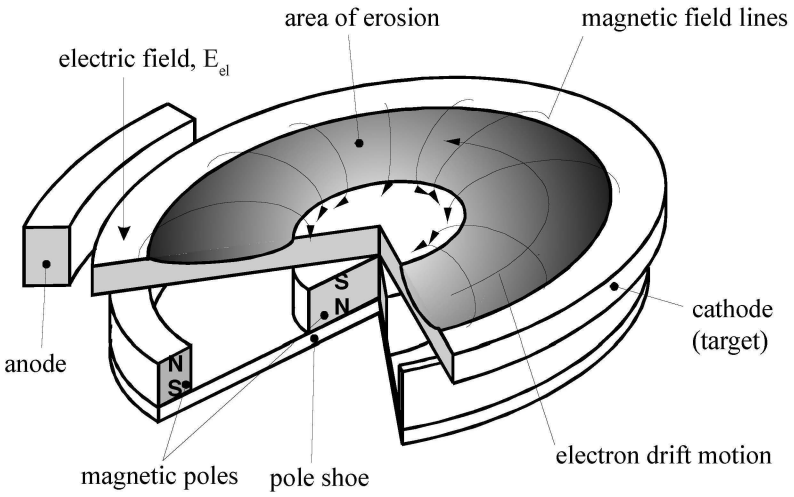

Fig. 2.3: A planar circular magnetron arrangement with a simplified demonstration of the field lines and the electron loop path [11].

$E \times B$ drift in magnetrons. For this reason, secondary electrons, which are emitted by the impingement of ions on the target, are trapped near the target in a loop path, which leads to higher ionization rates of the gas atoms in this region. As a consequence, the target erosion rate and, hence, the deposition rate can be increased significantly. There are several ways to layout the permanent magnets, e.g., circular, rectangular or square patterns. Due to the locally enhanced sputtering beneath the electron loop path, a characteristic erosion track on the target surface occurs [8].

By adaptation of the magnetic field layout, magnetron processes can be further distinguished. One of the most common implementations is the *unbalanced magnetron*. In this case, the outer magnetic poles are stronger than the inner ones, hence the magnetic field becomes irregular. The field lines point not only in a loop path but also towards the substrate and consequently the plasma is less defined as some of the electrons are

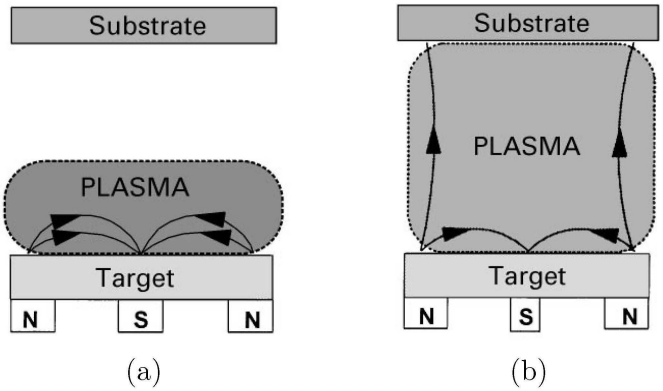

Fig. 2.4: (a) Conventional balanced magnetron configuration with loop-like field lines and (b) an unbalanced magnetron configuration with magnetic field lines extending towards the substrate [12].

guided away from the target region (Fig. 2.4). As a result, the plasma is extended to the substrate surface, which enables higher ion currents at the substrate as well as an increased particle flux, compared to conventional magnetrons [12].

2.3 Nucleation and film growth

The nucleation stage at the beginning of film formation is characterized by the processes of condensation and adsorption. Depending on its initial energy a sputtered atom will get reflected or adsorbed. In the latter case, the adsorbed atom (termed adatom) may diffuse on the surface until it is trapped at an energetically favorable spot, e.g., defects, atomic steps or impurities. Several forms of adatom diffusion can occur; they are shown in Fig. 2.5. With the progressive adsorption of atoms initially metastable clusters with high mobility are formed. Eventually these nuclei grow to a critical size and become stable on the substrate surface.

Continuing growth of the nuclei leads to coalescence of these clusters until a uniform film develops. The film growth can be classified in three modes, which are illustrated in Fig. 2.6. If the adsorbed atoms are bound stronger to each other than to the substrate, island formation, known as Volmer-Weber growth, is expected. Contrary to that, planar or so-called Frank-Van der Merwe growth is observed, when adatoms preferably interact with substrate atoms, in which case a monolayer covers the surface before a second layer is deposited. The third mechanism, termed after Stranski and Krastanov, is a combination of planar and island growth. Islands are formed on one or more previously deposited monolayers.

When different materials are used as substrates and targets, generally the mismatch at such heterogeneous substrate-film interfaces has a significant impact on the occuring growth mode. Metal-metal and metal-semiconductor systems show primarily the mixed

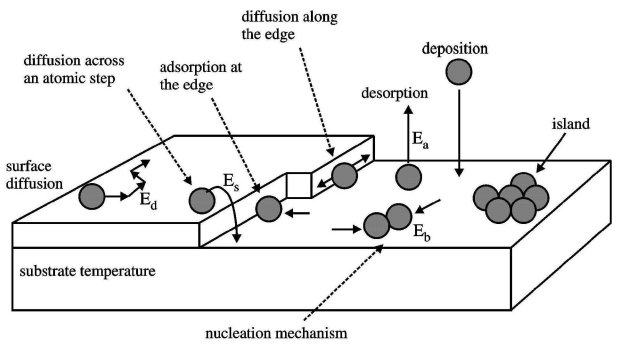

Fig. 2.5: Nucleation and diffusion processes during deposition [13].

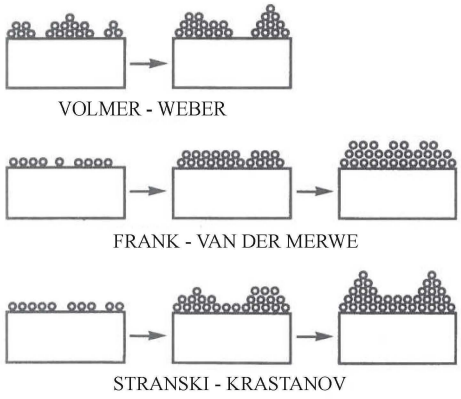

Fig. 2.6: The three main mechanisms of film growth [14].

Stranski-Krastanov growth [14], whereas for depositions of metals on polymer substrates Volmer-Weber film growth is observed, which is related to the divergent molecular configuration of polymers compared to metals. Furthermore, the surface roughness of polymeric substrates enhances island growth [15].

2.4 Microstructure

The film growth process and the film microstructure are highly influenced by preparation parameters during deposition. The idea to illustrate the relation between microstructure and certain deposition parameters in a so-called structure zone model (SZM) was introduced by Movchan & Demchishin [16] in 1969. Since then several SZMs have been established, of which some selected ones will be explained here. The first model focused on the substrate temperature with respect to the melting point, T_m, of the thin film material as the main impact during deposition [16]. Three characteristic zones were identified.

The first area, zone I, forms due to low temperatures ($< 0.3\ T_m$), where bulk diffusion is absent and only minor surface diffusion can be observed. As a consequence, shadowing effects predominate. This leads to tapered crystallites, which are separated by voids, resulting in an underdense film without any pronounced grain boundaries. Due to the limited diffusion, the size and orientation of the fibers is constrained to the initial clusters formed in the nucleation stage.

In zone II, at temperatures from $0.3 - 0.5\ T_m$, the mobility of the adsorbed atoms increases, which leads to grain boundary migration and recrystallization processes. Therefore, a columnar structure with defined grain boundaries throughout the whole film thickness is observed in this zone. The columnar grains are oriented in the direction of the impinging atoms, which is the thermokinetically favorable orientation for film growth.

In zone III, at substrate temperatures exceeding $0.5\ T_m$, grain coarsening and flattening of grain surfaces proceed, forming a dense film with equiaxed grains [17, 18]. Therefore, the columnar texture of zone II is neutralized with increasing temperature.

Thornton [17] proposed an adaptation of the SZM model, in which the inert gas pressure is included as an additional parameter (Fig. 2.7). It is observed that zone I broadens with increasing inert gas pressure. This can be explained by a decrease of the initial energy for diffusion of the adatoms due to more frequent collisions in the gas phase state. Further, Thornton introduced and described an additional region between zone I and II of the SZM by Movchan & Demchishin. In this so-called transition-zone (T-zone) surface diffusion of the adatoms rises by increasing the substrate temperature, in the range of $0.1 - 0.3$ for T/T_m. Thus, remaining voids are closed and more densely packed fibrous grains form. Furthermore, competitive growth among differently oriented crystals can be observed. Crystals with faces of minimal surface energy oriented perpendicular to the direction of

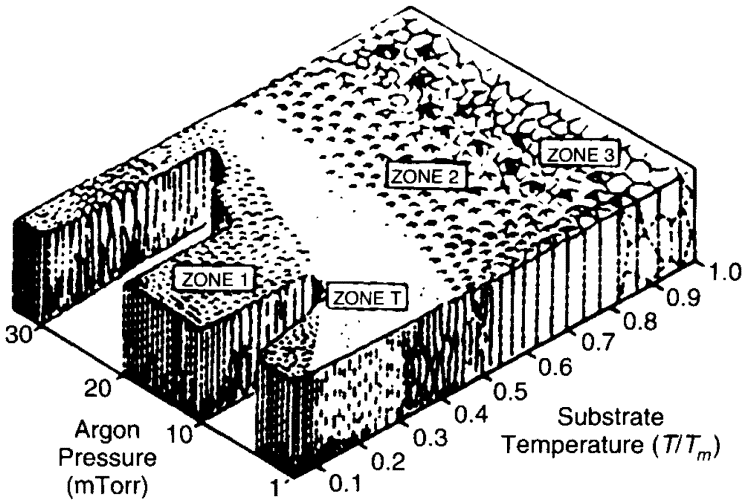

Fig. 2.7: The SZM by Thornton shows the influence of the temperature as well as the argon pressure on the microstructure evolution [8].

the atom bombardement show the tendency to incorporate more atoms and grow faster than crystals with higher surface energies. Therefore, these preferentially oriented crystals predominate in the coating and show an increasingly columnar structured texture with increasing film thickness [17].

In the model of Messier *et al.* [18] the inert gas pressure parameter was replaced by the substrate bias potential. Therefore, the energy of incident particles as well as thermal effects were taken into account, so that the effect of the mobility of adatoms, especially for zone I and T-zone structures, is described more accurately. In general, with increasing bias potential the dimension of the T-zone increases likewise.

2.5 Mechanical properties

2.5.1 Metal thin films on compliant substrates

The interface between film and substrate has a great impact on the deformation mechanisms of metal thin films deposited on polymer substrates. Therefore, to gain knowledge about the mechanical properties of metal thin films deposited on polymers, it is necessary to investigate the film-substrate couple as a whole material system. Moreover, the polymer strongly affects the plasticity and the fracture behavior of the deposited films. Thus, the influence of the polymer cannot be ignored when testing metal thin films for flexible electronic applications. One of the commonly used polymer substrates for research of flexible electronics is polyimide (PI), which shows higher stability against heat compared to other plastics such as polyethylene (PE) or polyethylene terephthalate (PET) [3].

It is required for flexible thin films to withstand tensile and compressive loads without fragmentation of the metal film. To obtain a high stretchability of flexible devices, the

thin films must exhibit high fracture strain, also termed crack onset strain (COS), and good adhesion. In recent years, nanoindentation and especially uniaxial tensile straining have become the main methods to investigate the mechanical properties of thin films on polymer substrates [3, 19].

For uniaxial straining a film-substrate sample is fixed between two grips of a straining device and is mechanically displaced along one axis. Uniaxial tensile testing has the advantage of being easily implemented and, in addition, can be combined with further *in situ* analysis techniques, e.g. 4 point probe (4PP) measurement to examine the electrical response during straining. Further, the film can be monitored under an optical microscope for cracks during straining. As a result, the elastic modulus, the yield stress and the stress-strain response are evaluated [3]. In regard to the deformation behavior, brittle and ductile thin films show different failure mechanisms. Fig. 2.8 exemplifies the difference in fracture behavior of a brittle film compared to a ductile one. Brittle thin films exhibit straight through-thickness cracks (STTCs), whereas in ductile films necking is found, which will be explained in more detail in the following section.

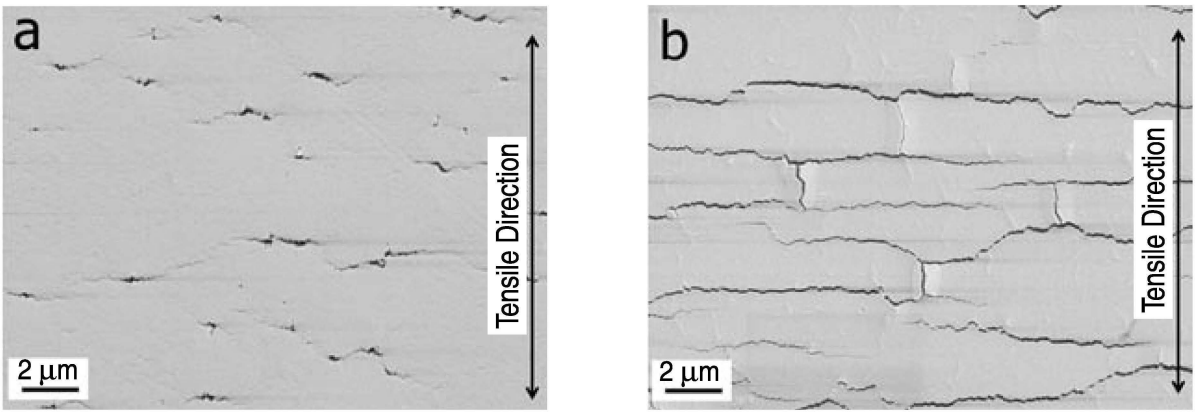

Fig. 2.8: Fracture behavior of (a) a ductile film (100 nm Cu on polyimide substrate), which only exhibits small cracks and necking, and in comparison to that, (b) a brittle film (100 nm Cr on polyimide substrate) with straight through-thickness cracks and buckles [3].

2.5.2 Deformation behavior of ductile films

The deformation behavior of a polymer-bonded ductile metal thin film significantly differs from a freestanding one as illustrated in Fig. 2.9. If a freestanding ductile metal film is strained in tension, it ruptures at very low strains due to local thinning of the film, which is known as necking. The formation of necks results from local plastic deformation, coupled with stress concentration at the narrow region, which again leads to higher local strains. In contrast to bulk material, more dislocations are able to escape at the free surfaces of the metal film and, as a result, hardening due to plastic deformation is less

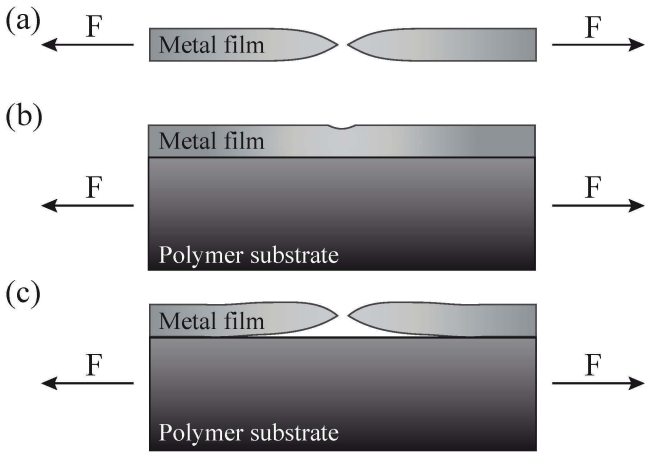

Fig. 2.9: Deformation behavior of (a) a ductile freestanding film, (b) well-adhered ductile film, which shows local thinning, and (c) a poorly adhered ductile film on compliant substrate (Figure based on [3]).

distinctive. Further straining locally thins out the film, until it ruptures perpendicular to the straining direction. This phenomenon is termed strain localization. As a consequence of the extremely small thickness-to-length ratio in thin films, the local elongation contributes very little to the overall failure strain, which is slightly above the elastic limit [20].

Contrary to freestanding films, strain localization can be retarded to higher strains if the ductile film is supported by a substrate. Depending on the interfacial strength between film and substrate three types of tensile behavior have been pointed out. If the adhesion is poor, failure similar to a freestanding film is observed, as delamination and necking facilitate each other at a single location. With increasing adhesion the film withstands higher strains before debonding and necking occur at multiple spots. When delamination can be totally suppressed by a high interfacial strength, the film can deform uniformly without rupture up to very high strains [20].

2.5.3 Deformation behavior of brittle films

A freestanding brittle film fractures by cleavage, which is the breaking of single arrays of atomic bonds with minor plastic deformation and without localized necking as illustrated in Fig. 2.10. STTCs are formed almost immediately when the sample is strained in tension. As no large local elongation occurs, the supporting substrate does little to prevent a brittle film from fracture [21]. Thus, the deformation behavior of a brittle film-compliant substrate system is very different to one of a polymer-bonded ductile film. Once the brittle film ruptures from direct loading, further cracks result from an interfacial shear stress, which is initiated by the primary elastic deformation of the film and elastic-plastic

deformation of the substrate. As the substrate is yielding more easily, load is transferred from the interfacial stress field to the film, where tensile stress is induced [22, 23]. The amount of cracks formed depends on the applied strain. With increasing strain the amount of cracks progressively rises until a saturation level is reached, at which no further cracks are formed. As a result, a minimal crack spacing is obtained that correlates with the critical interfacial length required for load transfer to rupture the film. Below that length of interface the interfacial shear stress is too low to induce fracture stress, which would lead to the formation of further cracks [24].

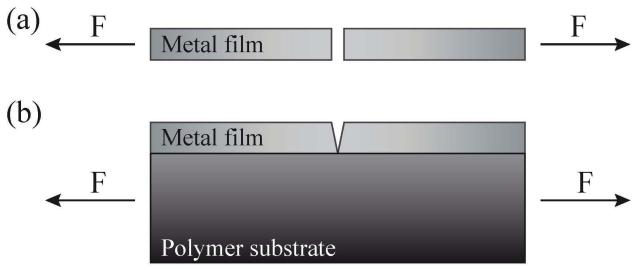

Fig. 2.10: Deformation behavior of (a) a brittle freestanding film and (b) a polymer-bonded brittle film, which ruptures by cleavage (Figure based on [25]).

2.5.4 Fragmentation testing

By monitoring the crack evolution during straining using, for example, an optical microscope, the damage of a strained film can be analyzed as a function of the applied strain. Therefore, it is useful to plot a so-called crack density curve, which has the charateristic shape of the schematic shown in Fig. 2.11. The crack density, which is inverse proportional to the crack spacing, is plotted over the applied strain or elongation. For brittle films the resulting curve typically reveals three stages of fragmentation.

Stage I is depicted by the crack initiation, which preferably starts at defects in the film or at regions of lowest fracture stress. The propagation of the primary cracks is perpendicular to the straining direction. At the beginning, the generation of new cracks is random due to the statistical distribution of defects within the film and the interaction of cracks is insignificant [19].

In stage II cracks propagate until the crack spacing reaches the critical interfacial length, which reduces further crack generation. New cracks are only formed in thin film fragments with dimensions of at least twice the critical length. Therefore, the slope of the curve flattens as the crack density is approaching a saturation level. Due to Poisson's ratio effects, which lead to compressive stress perpendicular to the straining direction, first buckles are formed [19, 27].

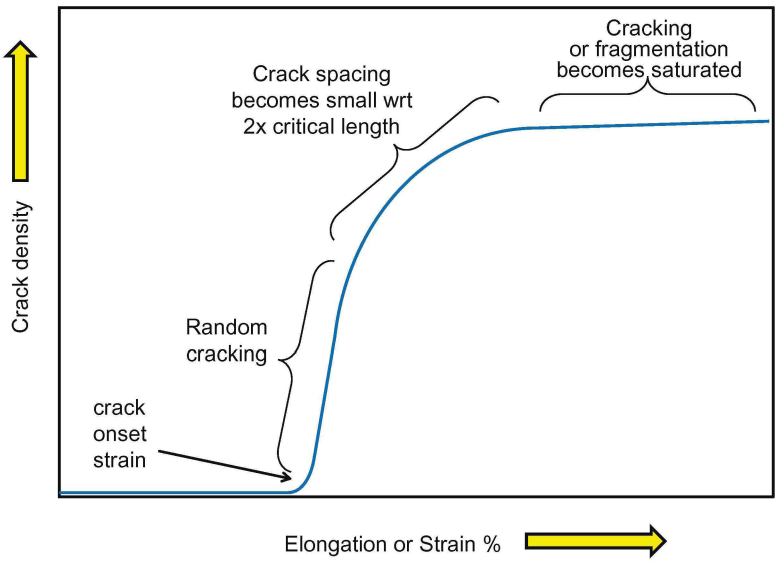

Fig. 2.11: Three stages of fragmentation testing [26].

In stage III delamination is the dominating failure mechanism. No cracks are generated, which results in the constant crack density as seen in Fig. 2.11. Further buckling occurs until the substrate ruptures.

Fragmentation testing has two advantages over other adhesion tests. First, with fragmentation testing there is no interaction of the sample with a third-body object, such as an indenter in the case of scratch tests. Second, it enables the direct determination of the COS very precisely as well as the crack density at saturation. This information can be used to calculate the adhesion energies at the film-substrate interface [19].

2.5.5 Performance enhancement of brittle films

As brittle films fracture by tensile stress, it is reasonable to induce compressive residual stress in order to enhance their deformation behavior during straining. Due to the internal compressive stress, additional energy is required to overcome the fracture strain of the film. Therefore, the COS can be significantly increased by inducing compressive residual stress in the film [28]. One way of inducing compressive stress during sputtering is to apply a bias voltage at the substrate, which accelerates the ions from the plasma towards the substrate and, hence, towards the growing film. This enhanced ion bombardment results in denser films and more defects are generated, which leads to the rise of internal compressive stress [29]. Another way to induce compressive stress is to prestretch the polymer substrate during deposition. When the sample is relaxed subsequently, residual compressive stress is introduced in the film [3].

2.6 Electrical properties

2.6.1 Metal thin films compared to bulk material

The electrical conductivity of metal thin films is usually lower than that of the corresponding bulk material. This trend is explained by three electron scattering phenomena, which operate simultaneously: (i) background scattering due to combined effects of phonons and point defects, (ii) scattering due to grain boundaries and (iii) scattering due to external surfaces [30]. In bulk material electrons are seen as freely moving particles, which are scattered mainly due to lattice vibrations, i.e. phonons. In metal thin films especially grain boundary scattering increases the electrical resistivity, due to a reduction in grain size with decreasing film thickness. In addition, effects due to the sample surface must be taken into account for very small film thicknesses. The electron mean free path is disturbed by the surface, at which the electrons are deflected inelastically [30].

2.6.2 *In situ* 4 Point Probe measurement

The capability of film-polymer composites to withstand stretching and bending without electrical failure is essential for the use as flexible electronics. Beside mechanical phenomena such as necking, cracking or delamination under tensile load, the electrical resistance is the main parameter determining the functional stability of metal thin films for flexible electronic applications. Thus, one technique widely used to determine electrical and mechanical behavior simultaneously is to perform uniaxial tensile tests in combination with 4PP measurements. In the 4PP test setup, the films to be strained are equipped with electrodes to determine the electrical conductivity throughout the sample in real-time (Fig. 2.12). This method allows to monitor qualitatively the cracking behavior of brittle films by measuring the electrical resistance as a function of the continuously applied strain.

The setup for 4PP probe measurements can be either a layout where the contacts are positioned separately within the gauge length of the film or a layout where the electrodes are incorporated in the grips of the straining device. The latter has the advantage that the strained part of the sample is not unnecessarily influenced, that there are no conductive pastes needed and that measurement conditions can be expected to be nearly the same for all samples [3, 31]. A more detailed explanation of the electrode-grip setup used for the experiments in this work is given in Section 3.4.1.

When straining a sample with *in situ* 4PP, it can be seen that the electrical conductivity of thin metal films is highly dependent on the mechanical load applied to the film-polymer composite.

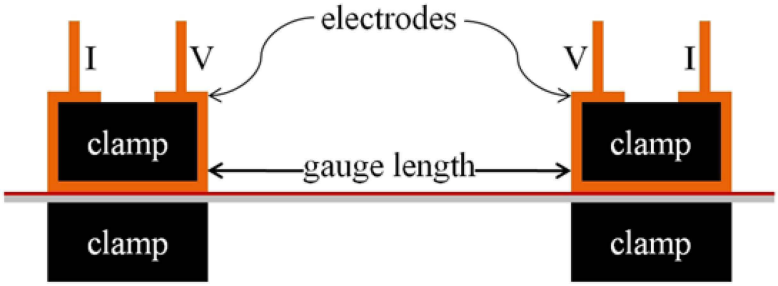

Fig. 2.12: Schematic overview of a tensile straining setup with *in situ* 4PP [32].

The initial resistance R_0 of a metallic thin film prior to straining is given by

$$R_0 = \rho \frac{L_0}{A_0} \ , \tag{2.1}$$

where ρ is the resistivity of the film material, L_0 is the initial gauge length and A_0 is the initial cross-section of the metal film. As the sample is strained, the initial resistance R_0 changes to

$$R = \rho \frac{L}{A} \ , \tag{2.2}$$

with $L = L_0 + \Delta L$ as the instantaneous gauge length and A as the instantaneous cross-section. As long as the film under tension is stretched in the elastic-plastic regime assuming that the volume of the film remains constant ($A \cdot L = A_0 \cdot L_0$), the ratio of R to R_0 takes the following form

$$\frac{R}{R_0} = \left(\frac{L}{L_0} \right)^2 = (1 + \epsilon)^2 \ , \tag{2.3}$$

where ϵ is the applied strain. The COS is determined when the resistance ratio $\frac{R}{R_0}$ deviates from the theoretical resistance due to significant structural modifications, e.g. the formation of cracks. As the evolution of $\frac{R}{R_0}$ does not follow any longer Eq. (2.3), the relative resistance increase can hardly be described by analytic formulas [33].

The measured value for the resistance $R_{0,\mathrm{meas}}$ of an unstrained thin film sample mounted in a straining device, such as the one shown in Fig. 2.12, consists of two parts: (i) the resistance of the film itself ($R_{0,\mathrm{samp}}$), which will be exposed to tensile strain, and (ii) a constant resistance part (R_{const}):

$$R_{0,\mathrm{meas}} = R_{0,\mathrm{samp}} + R_{\mathrm{const}} \tag{2.4}$$

During straining the measured resistance is given by

$$R_{\mathrm{meas}} = R_{\mathrm{samp}} + R_{\mathrm{const}} \ , \tag{2.5}$$

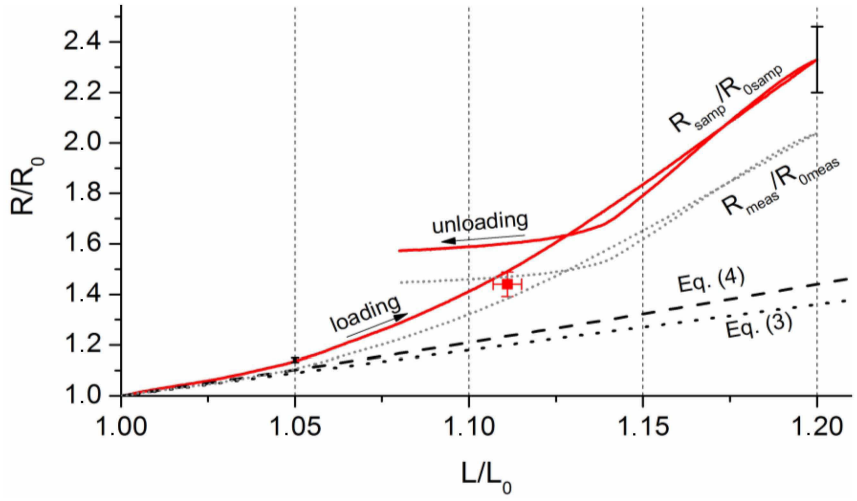

Fig. 2.13: A typical loading-unloading curve with *in situ* 4PP, which shows the relative resistance growth in relation to the relative elongation of the sample. The measured relative resistance ($R_{\mathrm{meas}}/R_{0,\mathrm{meas}}$) is depicted by the short dotted curve, whereas the solid red curve shows the corrected relative resistances ($R_{\mathrm{samp}}/R_{0,\mathrm{samp}}$). Eq. (2.3) (equivalent to Eq. (4) in the reference) is shown by the dashed line [31]. (The dotted line (Eq. (3)) is not discussed here in detail, but in Ref. [31].)

where R_{samp} is the resistance of the strained part of a sample.

The constant resistance part, R_{const}, is attributed to a contact resistance originating from the film under the grips, where it is not strained, and from the resistance of an optional conductive paste. Glushko & Cordill [31] showed that the constant resistance part is important for proper interpretation of the measured values and should only be neglected if $R_{0,\mathrm{samp}} \gg R_{\mathrm{const}}$. Otherwise, the resistance measured with the ohmmeter will be underestimated in regard to the actual resistance of the sample.

A typical resistance-strain curve of an *in situ* 4PP measurement during loading and unloading is shown in Fig. 2.13. The corrected relative resistance (red solid line) as well as the actually measured relative resistance (short dotted line) are depicted in the graph, which clearly shows the underestimation of the resistance growth if R_{const} is neglected. At the beginning of straining, the curve follows the theoretical line (dashed line), which illustrates the constant volume assumption from Eq. (2.3). At about 2 to 3 % strain the deviation of the relative resistance from this theoretical line indicates the COS, as crack formation is initiated. As cracking of the film continues, a substantial increase of the relative resistance is observed. During unloading, the resistance decreases with an almost identical slope as the loading curve until a plateau is reached, which demonstrates that the resistance growth is reversible to a certain extent. This reversibility can be explained on the one hand by the shrinkage of the viscoelastic polymer substrate and on the other hand by the partial closure of cracks. To which extent this relative resistance decrease occurs, depends primarily on the ability of the film to recover from fracture [33].

2.7 The molybdenum-rhenium system

The effect of rhenium on molybdenum in bulk material was first investigated in the 1950s [5, 6]. Geach & Hughes [5] studied the mechanical properties of different Mo-Re alloys and reported a remarkably high workability of different Mo-Re alloys at low temperature. Repeated rolling of an as-cast Mo-Re alloy with 35 at.% Re showed an overall reduction by more than 95 %, before cracking at the edges and on the surface of the sample occurred. Further investigations by Leichtfried *et al.* [34] yielded a decrease in the ductile-to-brittle transition temperature of Mo-Re alloys with increasing Re content. Although they could not identify an increase of tensile elongation due to the modest strain rates in the tensile tests, they found a change in fracture behavior from intergranular fracture for pure Mo to partially ductile fracture for 31.8 at.% Re alloys by performing Charpy impact tests. These initial studies suggested a ductilization effect of Re in Mo.

For higher Re contents ($>$ 35 at.% Re), an observed decrease in workability can be attributed to the presence of a brittle phase [34]. This suggestion is in agreement with the occurrence of an ordered, brittle σ-phase structure at approximately 30 at.% Re as illustrated in the phase diagram (Fig. 2.14).

In literature several theories have been proposed for the exceptional ductilization effect of Re on Mo up to the appearance of the brittle σ-phase [6, 34, 36–38]. Ductile behavior based on slip mechanisms was ruled out as a fundamental deformation mechanism. Slip would lead to earlier failure than observed, as the flow stress during tensile loading would exceed the fracture toughness, which would be lowered due to work-hardening effects. Instead, the ductility of Mo-Re alloys was explained by mechanical twinning. Twinning

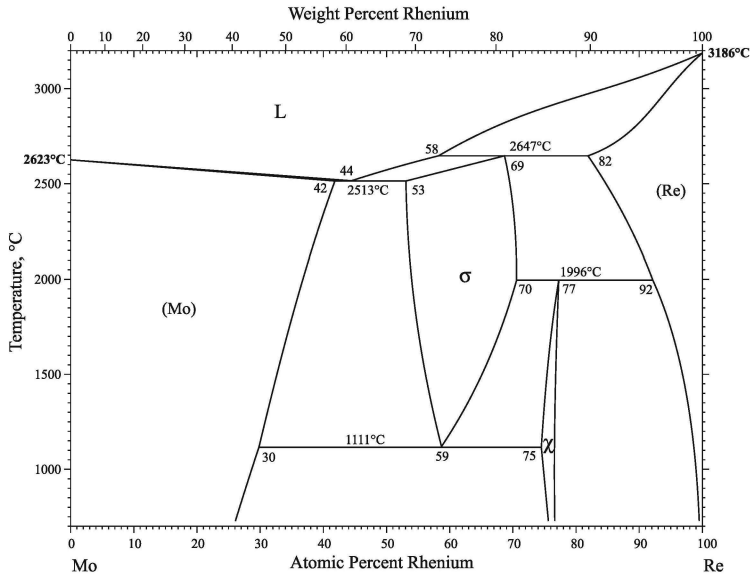

Fig. 2.14: The Mo-Re phase diagram [35].

occurred primary in grains with a 45° orientation to the load direction, thus, in the direction of maximum shear stress. Further, the Re content, the test temperature and the strain rate were the main influences observed [6]. More recently, computational studies by Gornostyrev *et al.* [36] on the Mo-Re system showed that deformation by twinning is activated at Re contents above 15 at.%. This is explained by a decrease of the stacking fault energy in the {112} plane. In addition, they assumed that the twinning mechanisms are accompanied by Re-enhanced dislocation mobility, which also affects the deformation behavior positively. Further, they showed that the covalent-like bonding character of Mo, which is primarily related to impurities in the bulk material and decisive for the brittleness of Mo, can be diminished through addition of Re. This is due to an increased solubility of interstitial impurities, e.g. oxygen or carbon, in the crystal lattice, or due to a change in segregation behavior of these impurities at the grain boundaries, or both [34, 36].

A study on the solid-solution softening in body-centered cubic (bcc) Mo alloys concluded that the dislocation mobility in Mo is improved by transition metals, such as Re or Pt, which increase the electron to atom core ratio in the crystal. Re and Pt enable the bowing of a double kink dislocation line, thus promoting dislocation nucleation gradually with solute content [37]. This plays an important role in the mechanical properties of Mo-Re alloys, as dislocation nucleation is known to be fundamental part in ductile deformation behavior [39]. Interestingly, the maximum of ductilization, in this study given as the minimum hardness values, was below the solubility limit for Re in Mo. Even before the σ-phase appears, solid-solution hardening is expected, which was explained by Medvedeva *et al.* [37] to the formation of Mo_3Re precipitates with the A15 (β-W) type structure. This highly ordered but metastable structure is made responsible for the ductilization limit, similar to the occurrence of the brittle σ-phase.

3 Experimental methods

3.1 Sputter deposition

The thin films investigated within this work have been deposited using a laboratory-scale unbalanced magnetron sputter deposition system containing three unbalanced magnetrons focused to the substrate holder. Two of the magnetrons were equipped with powder metallurgically produced targets of pure Mo and pure Re and one magnetron was kept idle. The rotatable sample holder was placed opposite to the targets, so that the vertical distance from the samples to the center of the targets was about 40 mm. The rotation speed of the sample holder was set with a control element to a value of 70 on its scale, which was equivalent to an actual rotation speed of about 52 rpm.

As substrate materials, 350 μm thick Si strips (21 mm $\times$ 6.5 mm) with {100} orientation and 50 µm thick sheets of PI (UBE Upilex®) with 50 mm $\times$ 50 mm in size were used. The films deposited on the Si samples were used for structural characterizations, whereas the PI substrate served as the compliant material for the tensile test samples. The Si samples were cleaned in an ultrasonic bath of ethanol for 10 min. The PI sheets were fixed with Kapton tape on the sample holder in the as-delivered condition, as an additional cleaning process with ultrasonic bath or with laboratory wipes would have generated undesired contamination and scratches.

The chamber was evacuated to a pressure of less than 2×10^{-3} Pa before feeding the chamber with 200 sccm of Ar gas resulting in a working pressure of approximately 1 Pa. The substrates were plasma etched prior to deposition by applying an asymmetric pulsed DC discharge of -290 V and 50 kHz for 2 min. In the subsequent deposition step, the Ar flow was reduced to 15 sccm, resulting in $\sim$0.38 Pa working pressure.

The composition of the deposited films was adjusted by varying the current applied to the targets. With a set current of 0.35 A on the Mo target and an altering current of 0 to 0.35 A on the Re target, the amount of Re in the thin film was varied. To produce pure Mo and pure Re films only the respective target was supplied with a current of 0.35 A. At least two deposition runs for each composition were conducted. The first deposition run was performed only with Si substrates and with deposition times between 12 and 18 min, in order to obtain films with a thickness of about 500 nm. For the second deposition run with Si and PI substrates, which were taped to the sample holder as shown in Fig. 3.1, the deposition time was set to about one minute, which resulted in thinner films with a thickness of approximately 50 nm.

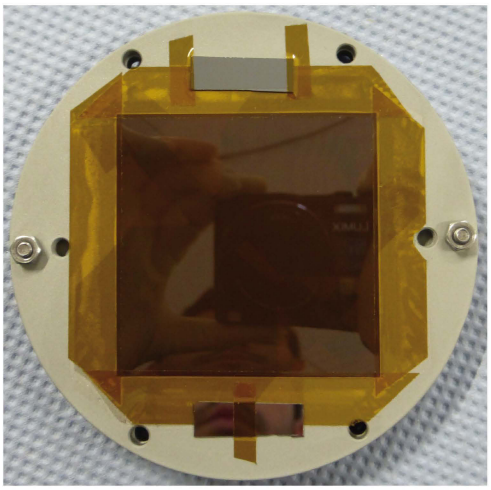

Fig. 3.1: Sample holder with Si and PI substrates attached.

3.2 Thin film characterization

3.2.1 Film thickness

The film thickness was obtained with a Wyko NT 1000 optical 3D white light profiling system. Therefore, a strip of Kapton tape was positioned in the middle of the Si substrate prior to the deposition and removed after the deposition process to determine the height difference between the uncoated and coated region. For measurements with an optical profilometer it is necessary to have a good reflectivity of the sample in order to obtain an interference pattern. This cannot be achieved with transparent materials such as polymeric substrates. Hence, a direct evaluation of the film thickness on PI substrates was not performed, but was indirectly determined from films deposited simultaneously on Si substrates (see Fig. 3.1).

3.2.2 Chemical composition

The chemical composition of the films on Si substrate was analyzed with an energy dispersive X-ray emission spectroscopy detector (EDX, Oxford Instruments INCA) attached to the scanning electron microscope (SEM, Zeiss Evo-50). Calibration was done using the built-in sensitivity factors. In order to avoid errors and influences due to a possible stimulation of the Si substrate by the electron beam when measuring very thin films, films for EDX measurement were produced with a thickness exceeding 450 nm.

3.2.3 Microstructure

To investigate occurring phases in the films, X-ray diffraction (XRD) measurements were performed with a Bruker-AXS D8 Advance diffractometer. All thin films were measured with the grazing incidence mode using Cu-K_α radiation with a wavelength of 0.154 nm.

The angle of incidence was fixed at 2 ° and the detector was moving every 1.2 s with a step size of 0.02 ° in a measurement range from 20 to 95 °. The recorded patterns were compared with reference patterns from the database of the International Centre for Diffraction Data (ICDD), which enabled a qualitative analysis of the thin film phase structures.

3.2.4 Sheet resistivity

The sheet resistivity of all films deposited on Si was measured with a 4PP by Jandel. For each specimen the resistivity was determined at the edges and in the middle of the sample to obtain a mean value of each sample. The four measurement tips were simultaneously brought in contact with the thin film without any mechanical loading of the film itself. As schematically shown in Fig. 3.2, the outer tips were supplied with a high impedance current, whereas the two inner tips measured the electric potential drop in between them. From the measured voltage, V, the bulk resistivity, ρ, and the sheet resistivity, R_s, can be calculated by the following equations, provided that the applied current, I, and the film thickness, t, are known [40]:

$$\rho = \frac{\pi t}{\ln 2}\left(\frac{V}{I}\right) \qquad \text{and} \qquad R_s = \frac{\rho}{t} \tag{3.1}$$

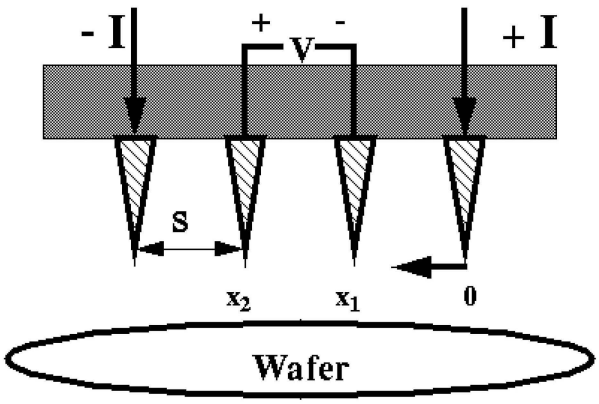

Fig. 3.2: Schematic layout of a 4PP measurement device [40].

3.2.5 Residual stress

Typically, a deposited film exhibits an internal film stress, which results in a slight curvature of the film-substrate composite. Depending on the residual stress state in the film, the film-substrate composite is bent to a varying extent. Compressive stress leads to a concave curvature of the film-substrate composite whereas from tensile stress a convex curvature can be expected. With wafer curvature measurements it is possible to quantify the residual stress in the films deposited on Si. The working principle of the measurement

device is based on the deflection of two initially parallel laser beams, which are pointed on the film-substrate composite. If the sample is curved due to residual stress, the reflected beams are no longer parallel. From this deflection of the laser beams conclusions can be made about the residual stress in the film. A more detailed description of the method is given in [11].

3.3 Heat treatment

In order to investigate any phase transformation, the ∼500 nm coated Si samples with a Re concentration within the range of 23 to 29 at.% were annealed in a vacuum furnace (HTM Reetz, base pressure $< 5 \times 10^{-4}$ Pa) at different temperatures and for variable length of time. The individual parameters for each heat treatment are given in detail in Table 1. The heat treatments were carried out consecutively with the same samples and, hence, the same films have been annealed several times. To avoid reactions of the Mo-Re films with the Si substrate, the annealing tests were conducted to a maximum temperature of 1000 °C. A heating rate of 20 K/min was kept unchanged for all annealing runs during the heating, which was only interrupted by holding period of 30 min at 250 °C in order to sustain a sufficient vacuum and a stable temperature level. Subsequently to each run, the annealed samples were investigated once more as to their microstructure with the X-ray diffractometer.

Table 1: Temperatures and holding times used in the annealing treatment tests.

Run	Temperature [°C]	Holding time [min]
1	500	15
2	500	60
3	900	15
4	1000	15

3.4 Tensile straining

3.4.1 Electro-mechanical testing

The theory behind electro-mechanical testing of films on compliant substrates has been described in Sections 2.5 and 2.6. A Tytron 250® Microforce Testing System (MTS) was used for uniaxial straining of the Mo-Re films. The *in situ* 4PP measurements during loading and unloading were performed with a multimeter (Keithley 2000), where the contacts were incorporated into the grips of the MTS straining device. A top-view of the test arrangement is shown schematically in Fig. 3.3. Similar to the 4PP for sheet

resistivity measurements, current is run through the outer two pins and the voltage across the sample is measured by the inner contacts. The contacts are built into the detachable top part of the grips, which is made of non-conductive material to provide a separate connection of the current injection contact and the voltage contact to the sample surface. This arrangement eliminates a so-called spreading resistance, which would add up to the resistance of the film and which would emerge from spreading of the current lines over the metal thin film volume [41].

The samples for the straining experiments with 5 mm × 35 mm in dimension were cut with a utility knife from the coated 50 mm × 50 mm sheets. The distance between the grips, thus, the actually strained part of the sample, was set in all MTS measurements to 20 mm.

The sample ends were placed on the fixed base parts of the grips and secured in position by the top part with two screws. The bottom ends of the contact pins for the *in situ* 4PP were slightly protrudent, which enabled a permanent direct contact with the sample. This has the advantage to provide always the exact same measuring geometry for each sample and no conductive paste is needed. Furthermore, the samples can be easily removed for subsequent microscopy analysis.

Prior to testing, the samples were slightly prestrained until a first increase of the acting force was recorded in order to avoid any slack at the beginning of straining. The control software of the MTS records the force over displacement, which is equal to time and strain, if the tests are conducted with a constant strain rate. On a separate computer the software for the multimeter was tracking the measured resistance over time. Thus, it was essential to start the software programs simultaneously. A minimum of three samples of each composition was tested and the resulting relative resistance curves were obtained by

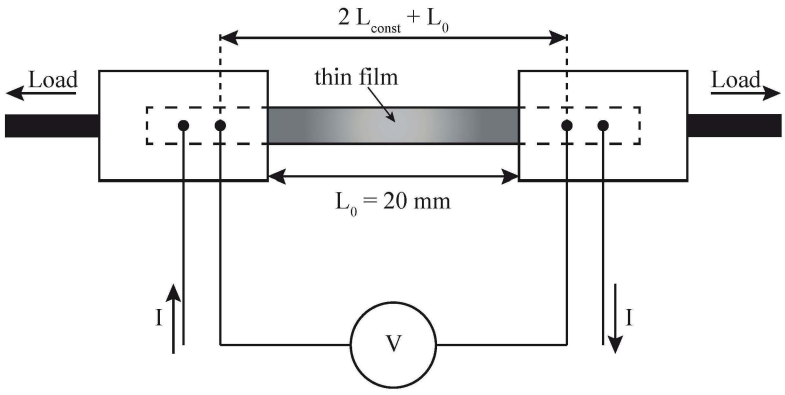

Fig. 3.3: Top-view of the experimental setup of the *in situ* 4PP measurement. For a better visibility in this scheme, the contact pins are plotted further apart than they actually are. The probing contact pins are located at the inner edges of the grips, i.e. $L_{\text{const}} \ll L_0$ and can, therefore, be neglected.

the arithmetic mean values from each tensile test.

While measuring the resistance, the samples were strained to 15 % with a constant loading rate of 5 µm/s for loading and unloading. After reaching maximum strain, the samples were unloaded to 5 % strain with the same loading rate in order to have a tension-free condition during disassembling of the test setup. The post-analysis of the fractured surface of the strained samples was performed with an optical microscope.

3.4.2 Fragmentation tests

In addition to the *in situ* 4PP tensile tests, fragmentation tests were conducted in order to investigate the crack growth behavior during straining as well as the COS independently from the resistance-strain curves. For this reason, the samples are strained in several steps and after each straining step a micrograph was taken.

The fragmentation tests were performed with an Anton Paar TS 600 straining device, which is equipped with the corresponding tensile stage control software. The samples of size 7 mm × 40 mm were clamped between two grips with a minimal distance of 22 mm. Similar to the electro-mechanical testing, the samples were prestrained to avoid any slack at the beginning of straining. This new position sets the initial gauge length, which slightly changes for each test. The initial gauge length has to be taken into account and, therefore, the value has to be implemented in the straining program. The loading rate was set to 10 µm/s. The software was programmed to perform smaller straining steps at the beginning of loading in order to obtain a good resolution in the region of stage I cracking, which was explained in Section 2.5.4. With progressive straining the steps were increased until buckling was reached at about 12 % strain.

The line interception method was used to obtain the crack spacing and consequently the crack density. Therefore, the micrographs from fragmentation testing were analyzed with the software ImageJ [42]. In every micrograph three lines were plotted perpendicularly to the direction of the cracks. By counting the points of intersection and measuring the length of the lines, an average value for the crack spacing could be determined [43]. The crack spacing, λ_{crack}, is defined as the ratio of the lines length, l_{lines}, to the number of intersection points, which is equivalent to the number of cracks, N_{crack}. The crack density, ρ_{crack}, is the reciprocal of the crack spacing (Eq. (3.2)).

$$\lambda_{\mathrm{crack}} = \frac{l_{\mathrm{lines}}}{N_{\mathrm{crack}}} = \frac{1}{\rho_{\mathrm{crack}}} \tag{3.2}$$

4 Results and discussion

4.1 Chemical composition

Given the information from the phase diagram (see Fig. 2.14), the formation of the brittle σ-phase is expected at a Re content of approximately 25 to 30 at.%. Since the aim of this work was to improve the ductility of Mo, only the compositional range up to ~30 at.% of Re was studied in detail. The samples were deposited with the current on the Re target set to 0 to 0.19 A. The resulting chemical composition for the $Mo_{1-x}Re_x$ alloy films is shown in Fig. 4.1, where an almost linear increase of the Re content with increasing current on the Re target is observed. An increase of 0.02 A in the Re target current resulted in an average increase in the Re content of ~2.9 at.%.

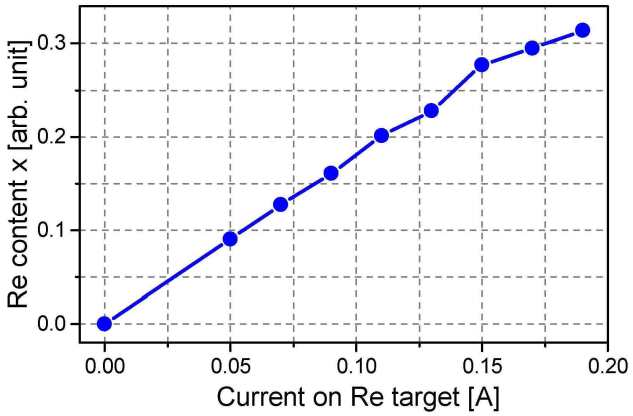

Fig. 4.1: The Re concentration in the deposited $Mo_{1-x}Re_x$ alloy films as measured by EDX is plotted as a function of the applied current to the Re target.

4.2 Microstructure

Fig. 4.2 shows the X-ray diffractograms of the 500 nm thick Mo-Re films on Si substrates with increasing Re content from the bottom to the top of the graph. The dashed lines indicate the standard peak positions of the reference patterns [44]. The XRD peak positions indicate a Mo (bcc) solid solution in the films with Re contents ranging from 0 to 23 at.%, while the Re thin film exhibits a hexagonal (hex.) microstructure. Slight peak shifts to higher 2θ angles with increasing Re content can be observed for the Mo-Re films with bcc solid solution structure. Due to the slightly lower atomic radius of Re (0.135 nm) compared to Mo (0.145 nm), the lattice parameter shrinks with increasing Re concentration.

The samples with a Re concentration higher than 23 at.% show a different microstructure as would have been predicted from the phase diagram. By comparing the measured peak positions with reference patterns it is observed that a metastable Mo_3Re phase forms

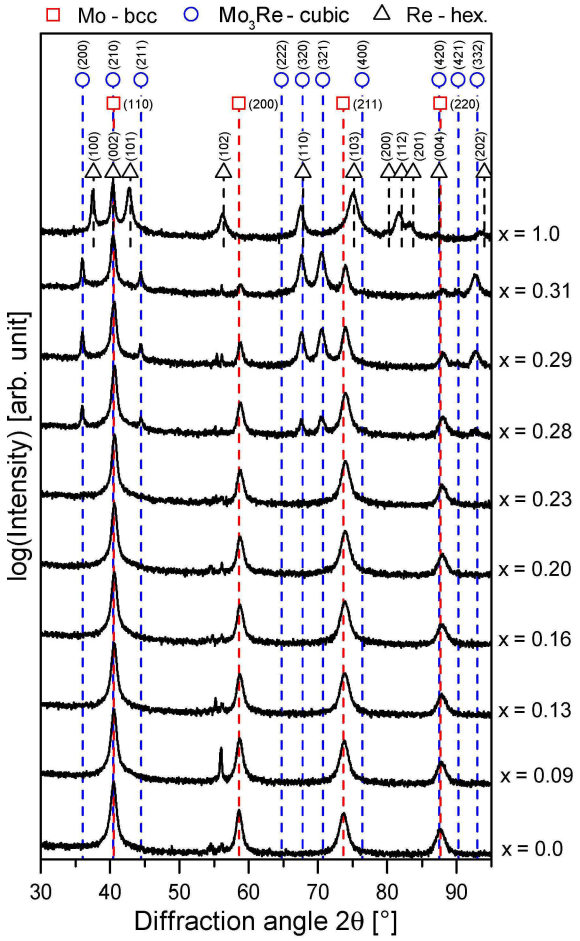

Fig. 4.2: X-ray diffractograms of the 500 nm thick $Mo_{1-x}Re_x$ films on Si substrates. The reference peak positions are according to [44].

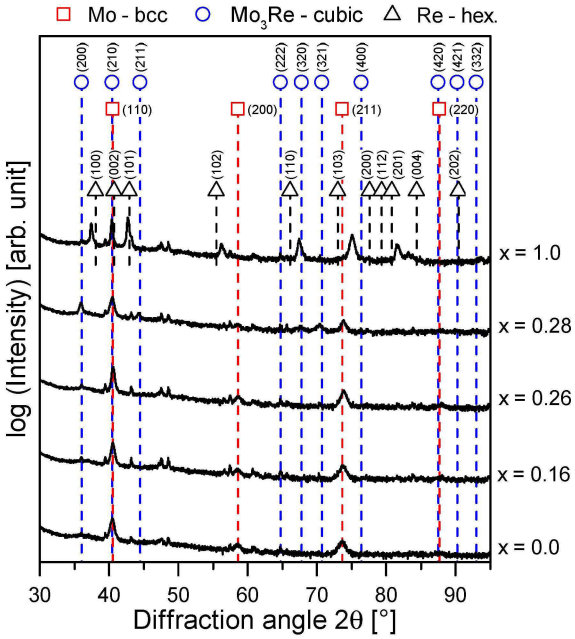

Fig. 4.3: X-ray diffractograms of the 50 nm thick $Mo_{1-x}Re_x$ films on PI substrates. The reference peak positions are according to [44].

rather than the anticipated σ-phase. According to literature, the Mo_3Re phase has the A15 (β-W) type structure and was observed at a Re concentration ranging from 25 to 35 at.% [45–47].

The X-ray diffractograms of the 50 nm thin films on PI substrate, as shown in Fig. 4.3, reveal a similar microstructure as the thicker films on Si substrates. The patterns of $Mo_{0.84}Re_{0.16}$ and $Mo_{0.77}Re_{0.23}$ match the peaks of Mo solid solution, whereas the pattern of the $Mo_{0.72}Re_{0.28}$ film is in good agreement with the reference pattern of the Mo_3Re phase. Note that the relative intensities of the peaks are smaller due to the reduction of the probed volume within the film and the smaller grain size in the thinner films. Further, the influence of the polymeric substrate can be noticed by the slight increase in background intensity at lower 2θ angles.

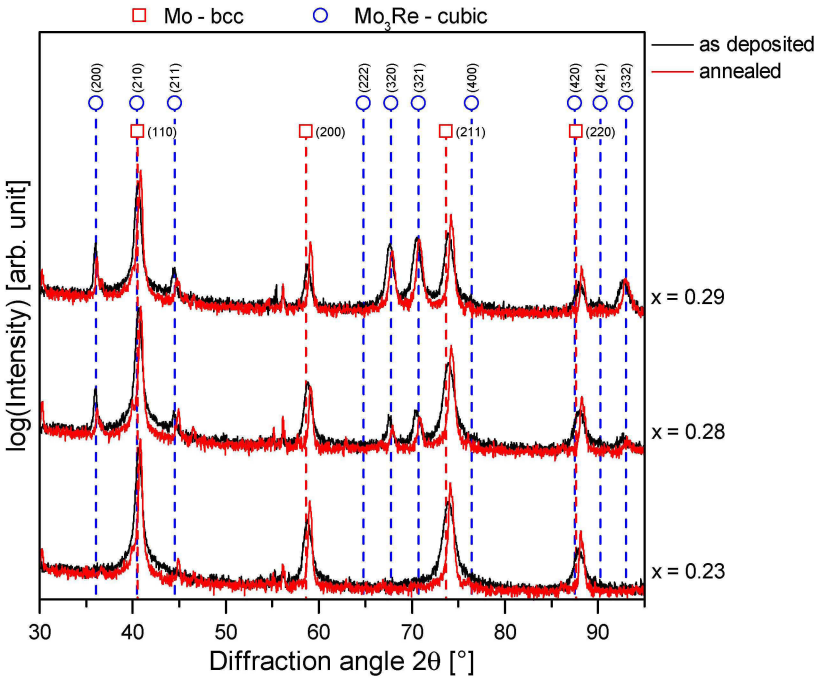

Fig. 4.4: X-ray diffractograms of the $Mo_{1-x}Re_x$ films with x = 0.23, 0.28 and 0.29 in the as-deposited state and after annealing to 1000 °C for 15 min.

4.3 Annealing tests

As the Mo_3Re phase in the Mo-Re system is known to be metastable [37, 38, 45, 46], annealing tests were performed in order to investigate its stability in the deposited Mo-Re films at elevated temperatures. The results from the last annealing run, where the samples were heated to 1000 °C, are shown in Fig. 4.4 and compared to the XRD patterns of the as-deposited films. Only a slight shift to higher 2θ angles of the peaks associated to the Mo_3Re can be noticed, which indicates that the A15-structured phase is stable up to these temperatures. Given the high melting points of Mo and Re of 2623 °C and 3186 °C [35], respectively, the high stability of Mo_3Re (A15) is plausible and should be validated with further investigations including computational studies. However, for the present work, i.e. Mo-Re films on polymer substrates, such temperature ranges are beyond the focus.

4.4 Sheet resistivity

The results from the 4PP Jandel sheet resistivity measurements are illustrated in Fig. 4.5. The unalloyed Mo film shows the lowest value of about 20 $\mu\Omega$cm, which is still about four times higher than the value for bulk material (5.2 $\mu\Omega$cm [48]). Even though lower values of approximately 10 $\mu\Omega$cm for 300 nm and 500 nm Mo films were reported in literature [49], the measured values seem reasonable considering that the substrates where not heated

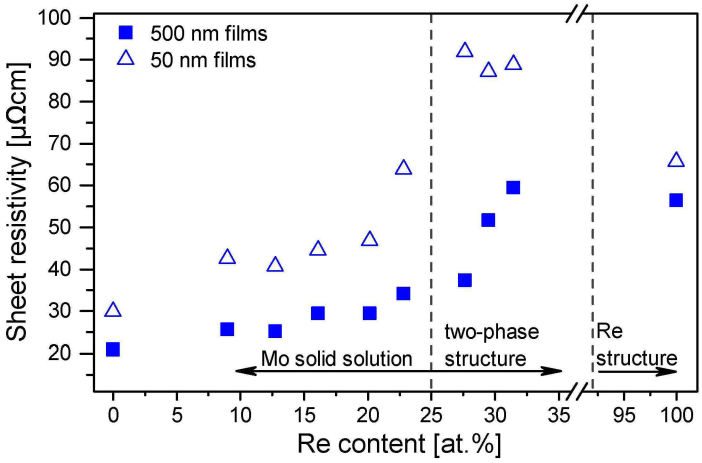

Fig. 4.5: Sheet resistivity of the 50 and 500 nm thick Mo-Re films measured on Si substrates.

during deposition as it was done in other studies. The additional heating during deposition is enhancing diffusion processes in the growing films, which typically results in a reduced defect density [14].

The deviation from the bulk material value can be attributed to the highly disordered microstructure in thin films, which leads to a higher sheet resistivity due to electron scattering at point defects and grain boundaries [49]. Alloyed atoms cause a deviation of the lattice parameter and can change the local charges in the lattice due to a different number of valence electrons. Therefore, the probability of electron scattering rises with an increasing amount of the added solute. For two-phase alloys, in many instances, it was observed that the total resistivity is the sum of the resistivity of each component, which can explain the notable resistivity increase as the two-phase structure is formed [50].

The resistivity measurements of the 50 nm films (Fig. 4.5) show a similar trend as the increase in resistivity for the two-phase alloys is clearly visible. By tendency, thinner films exhibit higher resistivity values due to smaller grains containing more defects and especially a higher volume fraction of grain boundaries in the films compared to the thicker ones [49].

The measured sheet resistivity of the Re film is about three times higher compared to the literature value of 18.8 $\mu\Omega$cm [51] but is still lower than the one of the two-phase structure.

4.5 Residual stress measurements

The results of the residual stress measurements according to the wafer curvature method are shown in Fig. 4.6. All measured samples except for the Re sample (85 MPa) show compressive stress, which is negative by convention. For the 500 nm Mo-Re films, the lowest internal compressive stress of -151 MPa is detected for sample $Mo_{0.84}Re_{0.16}$ and

the highest value of −823 MPa is measured in $Mo_{0.71}Re_{0.29}$. The compressive stress in the Mo-Re films can be explained by several factors. On the one hand, the incorporation of impurities, such as oxygen or carbon, at lattice defects are responsible for elevated internal compressive stress and, on the other hand, the applied bias potential at the substrate generates more defects.

Taking a closer look at the value for Mo and in comparison to the compressive stress values of the solid solution samples, a diminished compressive stress level is observed for the alloyed films. This could correlate with the advanced solubility of interstitial atoms, when Re is added to Mo as reported in a study on Mo-Re bulk material [36]. A diminished influence of the interstitial atoms could result in a stress relief in these films. Contrary to that, the samples with the Mo_3Re phase exhibit the highest compressive stresses, which are even higher than for the Mo film. Presumably this is related to the A15-structured precipitates, which hinder stress relaxation processes [37].

The residual stress is overall higher for the 50 nm films with a maximum residual stress of −5.4 GPa found for the Mo thin film. The lowest residual stress in the alloy films was measured for $Mo_{0.87}Re_{0.13}$ with a compressive stress of −1.8 GPa. For the films of 50 nm thickness, the outcome of the wafer curvature measurements should be regarded with some reservation. As the films are very thin, the resulting curvature of the film-substrate composite is marginal, which increases the error of the measurement significantly. Therefore, it is feasible to consider only the more reliable results of the thicker films and to assume a similar trend for the thinner films. However, it is known that thinner films exhibit higher residual stress due to an increased defect density in those films [52].

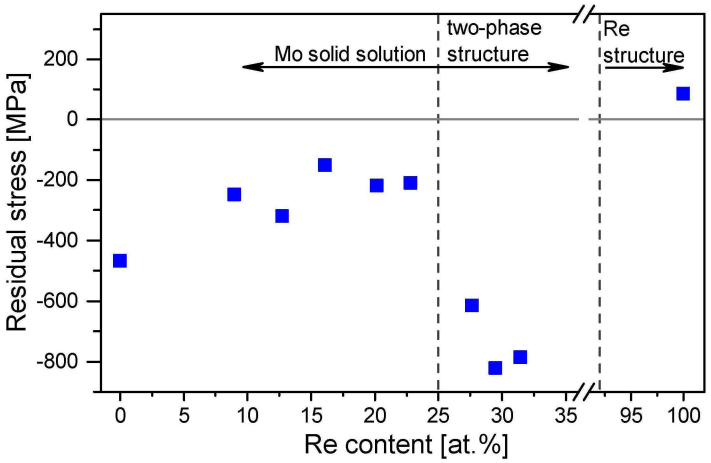

Fig. 4.6: Residual stress of the 500 nm thick films on Si substrate.

4.6 Electro-mechanical behavior

4.6.1 *In situ* 4PP tensile tests

The relative resistance, R/R_0, of the Mo and the Re samples with 50 nm in thickness is plotted as a function of the applied strain in Fig. 4.7. The dashed line indicates the increase of the theoretical resistance according to the constant volume assumption from Eq. (2.3). Consider that R_{const} is neglected in all relative resistance to strain curves, as it is sufficient to plot the measured relative resistance, $R_{\text{meas}}/R_{0,\text{meas}}$, for comparison of the trends.

Up to about 1 % strain, both, the Mo and the Re films, follow the theoretical line. After exceeding 1 % strain, the slope of the Mo resistance curve deviates significantly from the theoretical line as the relative resistance increases rapidly. In contrast to the sharp increase of the Mo sample, the Re thin film exhibits just a slight resistance increase after ∼1.7 % straining. From the electro-mechanical response of the Mo and Re film it is evident that the deformation behavior of these two films differs considerably. The micrographs of the strained films, shown in Fig. 4.9a and j, confirm this notion. The Mo thin film shows typical brittle fracture behavior with distinct STTCs perpendicular to the straining direction. Further, buckling of the Mo thin film can be clearly seen indicating that the saturation level of the crack density is reached. The buckles are aligned parallel to the straining direction and are formed due to the compressive stress, which develops according to Poisson's ratio effects. On the other hand, the micrograph of the Re film exhibits a more ductile behavior. In the Re film the cracks grow in zigzag ways and do not spread throughout the whole surface of the film. It should be noted that the dark dots, seen in the micrograph of Re (Fig. 4.9j), presumably originate from Re oxides, which are formed inevitably during the testing and analyzing process as the film was exposed to ambient atmosphere. As these oxides occur over time and only at the surface of the film, it is expected that their influence on the deformation behavior is negligible.

Studying the resistance-strain curves of the Mo-Re alloy thin films (Fig. 4.7) containing only solid solution, it can be seen that the COS is increased with increasing amount of Re. Each sample shows enhanced deformation behavior compared to Mo, which is also demonstrated in the micrographs Fig. 4.9b-f by the gradually changing crack pattern. The films containing 20 and 23 at.% Re even exceed the COS of the Re sample. However, their increase in relative resistance is much steeper than that of Re. Therefore, it can be concluded that, if Re is alloyed to Mo films, the COS can be shifted to higher strains - in the case of the $Mo_{77}Re_{0.23}$ to about 2.5 % - but the formation of far-reaching cracks is still observable (Fig. 4.9b-f). The micrograph of $Mo_{0.77}Re_{0.23}$ (Fig. 4.9f) indicates that compared to the Mo sample the cracks are deflected stronger and they spread in a wavy

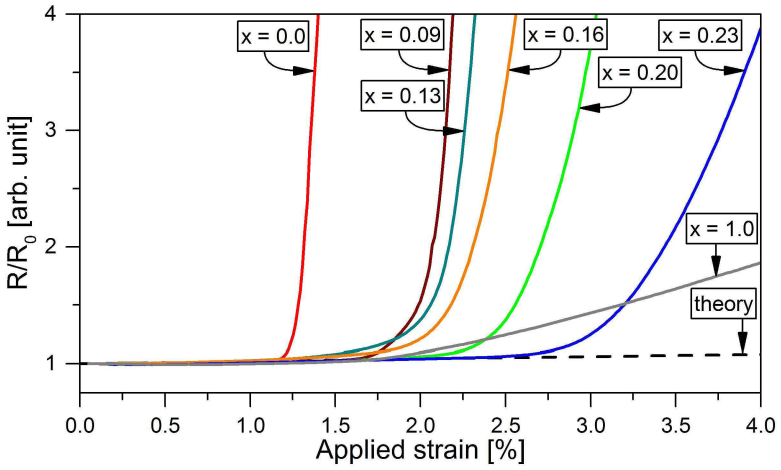

Fig. 4.7: Mean relative resistance curves in regard of the applied strain of the $Mo_{1-x}Re_x$ films with x = 0 and 1 as well as $0.09 \leq x \leq 0.23$.

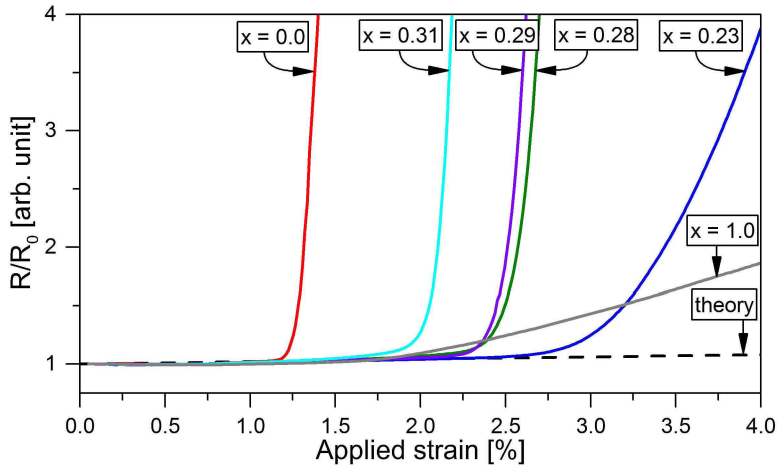

Fig. 4.8: Mean relative resistance curves in regard of the applied strain of the $Mo_{1-x}Re_x$ films with x = 0 and 1 as well as $0.23 \leq x \leq 0.31$.

crack path. Nevertheless, the crack propagation cannot fully be suppressed, which again leads to long cracks throughout the film. As a result of these long cracks, there is a greater increase of the relative resistance compared to the Re films. Further, it is observed that at 15 % strain, buckling is significantly less pronounced in the alloyed films than it is in Mo. This enhancement of the electro-mechanical behavior results from the ductilization effect of Re. Several effects have been described for bulk materials, which can be assumed to be also active in the Mo-Re thin films. A higher dislocation mobility as well as the less pronounced influence of impurities in the film seem to be the main reasons for the improvement of the COS in the films with 23 at.% Re [34, 36, 37].

In Fig. 4.8 the resistance-strain curves from the *in situ* 4PP tensile tests of the samples with a Re content of 23 at.% and higher are plotted together with the results from the Mo and Re samples. Compared to the solid solution samples with a maximum Re content of 23 at.%, it depicts a reversed trend of the COS for the two-phase samples, even though

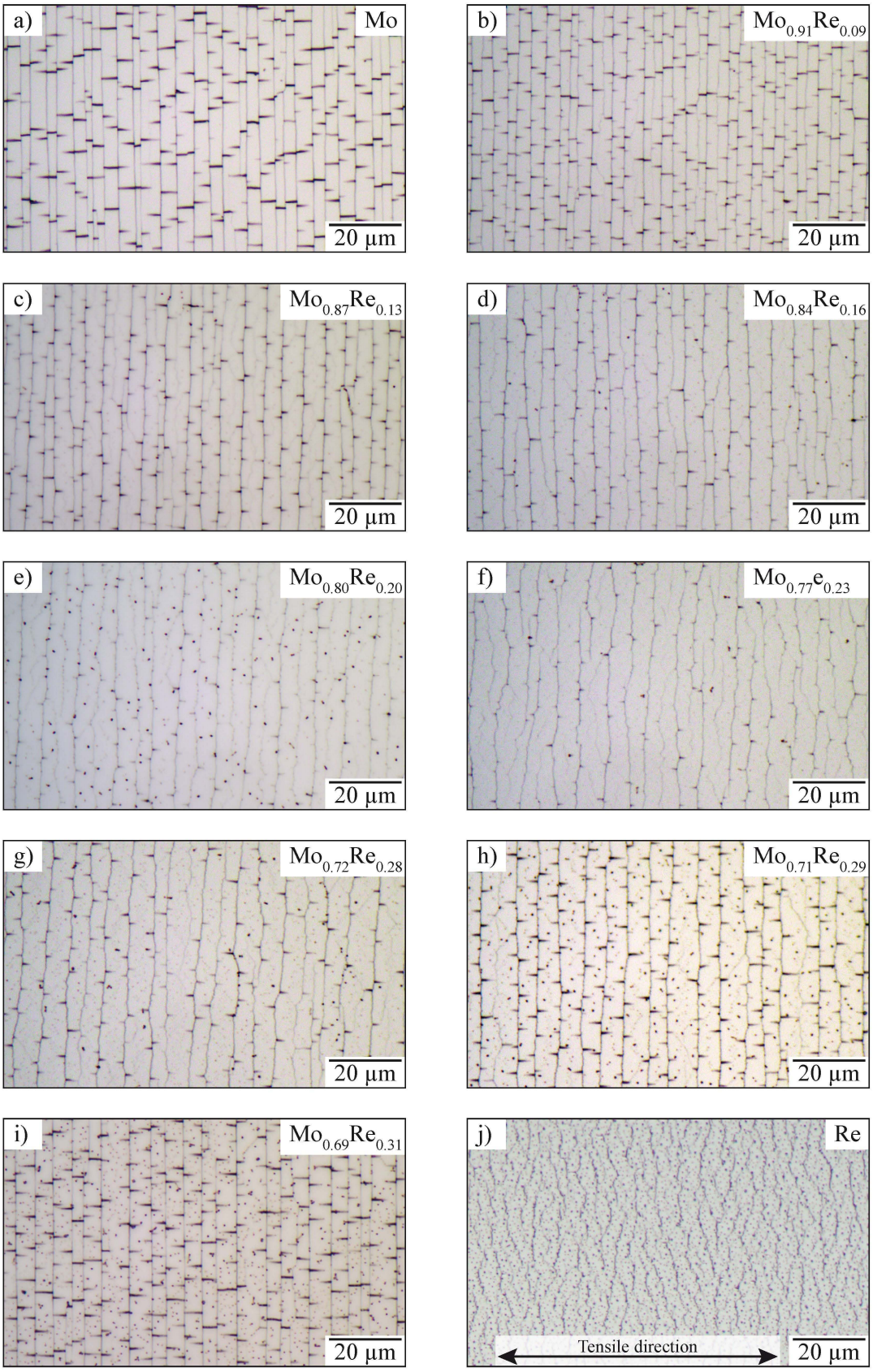

Fig. 4.9: Micrographs recorded after uniaxial tensile straining to 15 % strain showing the crack behavior of (a) Mo, (b-i) the $Mo_{1-x}Re_x$ films and (j) Re (strained to 12 % strain).

more Re is alloyed. For example, the $Mo_{0.69}Re_{0.31}$ film fails at approximately the same COS as the film containing only 9 at.%. Comparing the micrograph of the $Mo_{0.77}Re_{0.23}$ sample with the one of the $Mo_{0.69}Re_{0.31}$ (Fig. 4.9i), it is also apparent that the deformation behavior has changed. In the $Mo_{0.69}Re_{0.31}$ film the shape of the cracks evidently resembles the one of the Mo film with STTCs and significant buckling, instead of branched cracks and less pronounced buckling, which can be seen for $Mo_{0.77}Re_{0.23}$. This degradation is most likely due to the phase constitution in the films. From the XRD results it was concluded that a metastable phase above the limit of 23 at.% Re appears. This metastable phase is composed of the close packed A15 structure, which is expected to contribute to a hardening effect as described in Section 2.7. If this phase hinders dislocation motion and, therefore, ductile deformation, it can be suggested that the crack formation is mainly caused by cleavage instead of necking.

4.6.2 Crack density measurements

As an example, the micrographs from the fragmentation test of $Mo_{0.77}Re_{0.23}$ are shown in Fig. 4.10a-f, which give a clear impression of the crack evolution depending on the applied strain. Stage I cracking is seen in Fig. 4.10b and c, which is characterized by crack initiation. In Fig. 4.10d-f further cracking occurs until first minor buckles are observed as seen in Fig. 4.10f.

From the micrographs the crack density curves are obtained which are depicted in Fig. 4.11. The crack density curves reveal that the Re film can withstand higher strains

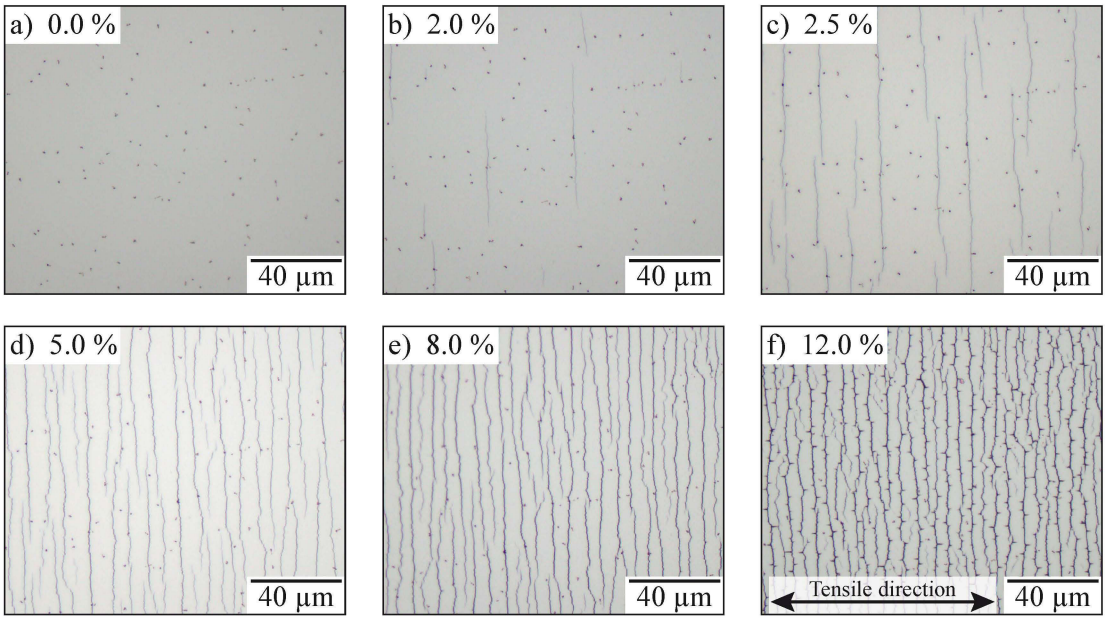

Fig. 4.10: Micrographs of $Mo_{0.77}Re_{0.23}$ recorded during the fragmentation test at (a) 0.0 %, (b) 2.0 %, (c) 2.5 %, (d) 5.0 %, (e) 8.0 % and (f) 12.0 % strain.

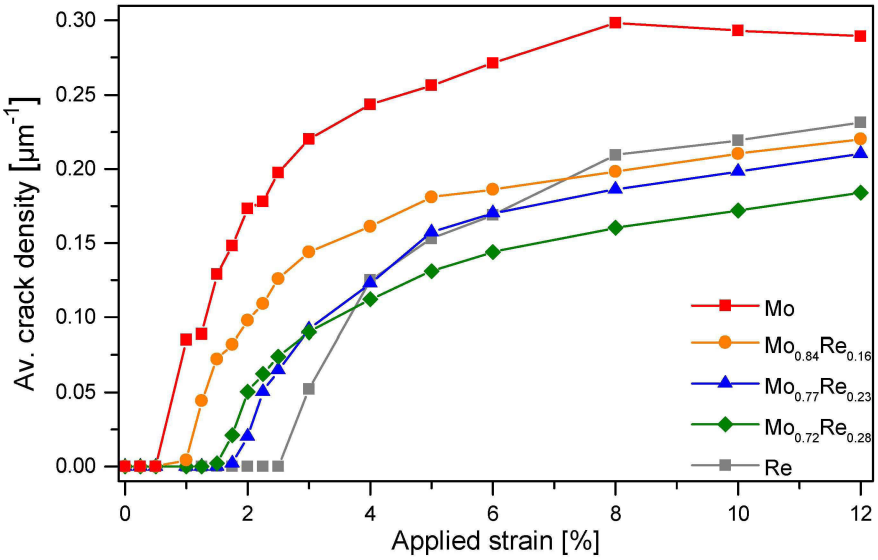

Fig. 4.11: Crack density curves of the Mo, $Mo_{0.84}Re_{0.16}$, $Mo_{0.77}Re_{0.23}$, $Mo_{0.72}Re_{0.28}$ and Re films.

than the Mo film before cracks start to form, which is in agreement with the *in situ* electro-mechanical tests. The COS of 2.5 % of the Re thin film is slightly higher, whereas the COS of Mo thin film is about the same.

Furthermore it can be seen that the slopes of those two systems differ with a steeper slope of the Mo sample. At the beginning of cracking, the Mo film features an average crack density that is almost twice as high as the one of the Re film, i.e. cracks are formed easier and to a much greater extent in Mo films.

Fig. 4.11 further shows the crack density curve of the $Mo_{0.77}Re_{0.23}$ sample, which exhibited the highest COS during *in situ* 4PP tensile tests, as well as the results from the Mo samples containing 16 at.% and 28 at.% Re. As can be seen from these curves, again the maximum COS of the alloyed samples is found for $Mo_{0.77}Re_{0.23}$ at about 1.75 % strain. The thin films containing 16 at.% and 28 at.% Re reveal lower COS values of about 1.0 % and 1.5 % strain, respectively. Overall, the COS values detected during the fragmentation tests are lower compared to the values from the *in situ* 4PP tests. The reason for this probably lies in the slightly different sample geometry and the utilization of a different testing device.

Contrary to measurements of the relative resistance, the Re sample appears to sustain higher strain than the $Mo_{0.77}Re_{0.23}$. It must be noted that this allegedly superior behavior of the Re film could originate from the difficulties during the micrograph analysis. Due to the evaluation of the crack density via optical methods it is hardly possible to detect necks and small cracks in the ductile Re film at the beginning of failure. But these necks and fine cracks could play an important role as they affect the electro-mechanical behavior of the film. For example, they could be responsible for the slight increase of the relative

resistance of Re observed during the *in situ* 4PP tests, but they are without influence on the fragmentation tests as they pass undetected.

Taking a more precise look at the saturation levels of the crack density curves, it is observed that Mo shows the highest crack density of about 0.30 cracks/μm. At the corresponding strains, the crack density values of the alloyed samples are notably lower and vary from approximately 0.15 to 0.20 μm^{-1}. Yet, it seems that these films have not fully reached a saturation level as seen for Mo. There is still a visible increase of the crack density in the range from 8.0 to 12.0 % strain, which concludes that the films are more ductile and the saturation of the crack density is probably shifted to higher strains. However, no information about the saturation level can be given because the PI substrate ruptured before the saturation level of the Re-alloyed films was reached.

The crack density curves also reveal that at strains above 4.0 % more cracks are formed in the Re sample than in the $Mo_{0.72}Re_{0.28}$ sample which showed a two-phase structure. Above 8.0 % strain even the other Mo-Re samples with solid solution microstructure show lower crack density values than the Re films. In the case of the $Mo_{0.72}Re_{0.28}$ film, this conjuncture is most likely related to the presence of the close packed A15-structured phase. Even though crack onset is not enhanced by its appearance, it can be assumed that its hardening effect hinders further crack formation at elevated strains. If so, this strengthening leads to an increased critical interfacial length, which is needed to induce cracks in the Re-alloyed Mo films.

5 Summary and conclusions

Within this thesis, the influence of Re alloying on the electro-mechanical behavior of Mo thin films deposited on PI substrates was studied. Therefore, $Mo_{1-x}Re_x$ thin films with a varying Re concentration in the range from x = 0.0 to 0.31 were synthesized by magnetron sputter deposition.

Microstructure analysis via X-ray diffraction revealed a single phase Mo-Re solid solution for all Mo-Re films with a Re content up to 23 at.%. Above that concentration, the alloyed films exhibited a second phase, which was determined as the metastable Mo_3Re phase. As the Mo-Re films containing the Mo_3Re phase showed a higher sheet resistivity than the solid solution films, this observed increase in sheet resistivity was associated with the change in microstructure.

In order to test the electro-mechanical behavior of the Mo-Re thin films on PI substrates, tensile tests with *in situ* 4 point probe measurements were conducted. The Mo film failed at 1 % applied strain, while the Mo-Re films were electrically as well as mechanically still intact. The highest fracture strain of about 2.5 % was observed for the Mo-Re sample containing 23 at.% Re, which exhibited an almost three times higher crack onset strain than the Mo film, clearly verifying the enhancing ductilization effect of Re when alloyed to Mo. Compared to the Mo film, the relative resistance increase for the $Mo_{0.77}Re_{0.23}$ was found to be less pronounced, also indicating a more ductile fracture behavior. Furthermore, the micrographs of the strained films revealed a significant change in the crack pattern of the films. The brittle Mo films exhibited straight-through thickness cracks and buckling at low strains, whereas the zigzag crack pattern for the Re alloyed films emphasizes the improved ductility. Additional fragmentation tests with *in situ* optical observation showed similar results. The crack density curves, which were obtained from these tests, indicated an improved deformation behavior with crack onset strain values shifted to higher strains when Re is alloyed, showing once more a maximum for $Mo_{0.77}Re_{0.23}$. Further, the Re alloyed films exhibited a decreased saturation level of crack density in comparison to the brittle Mo film.

Despite the observed enhancement, adding an excessive amount of Re leads to a degradation of the electro-mechanical response. Re concentrations above 23 at.%, at which the Mo_3Re phase forms, have an unfavorable effect on the microstructure and, therefore, on the fracture behavior of the Mo-Re films. All those films showed a significant decrease in fracture strain, even though they exhibited higher compressive stress than the solid solution thin films, which usually leads to a beneficial deformation behavior during tensile straining. This can be explained by a hardening effect in the films as the Mo_3Re phase forms, which was observed to hinder dislocation motion and, therefore, decrease the ductility of the films [37]. This leads to the conclusion that there exists an optimum amount

of Re in the Mo-Re film, which leads to a significant enhancement in the deformation behavior.

Considering an almost three-fold increase in the fracture strain measured for $Mo_{0.77}Re_{0.23}$ compared to Mo, the utilization of Mo-Re instead of Mo films for flexible display applications is a promising strategy in order to prevent easy brittle fracture of these functional thin films.

References

[1] D. Lupo, W. Clemens, S. Breitung, K. Hecker, OE-A Roadmap for Organic and Printed Electronics, Springer US, Boston, USA, 2013, pp. 1–26.

[2] W. S. Wong, A. Salleo (Eds.), Flexible Electronics: Materials and Applications, Springer Publishing Company, New York, USA, 2009.

[3] M. J. Cordill, JOM 62 (6) (2010) 9–14.

[4] T. Jörg, M. J. Cordill, R. Franz, O. Glushko, J. Winkler, C. Mitterer, Thin Solid Films 606 (2016) 45 – 50.

[5] G. A. Geach, J. Hughes, in: Proc. 2nd Plansee Seminar, Reutte, Austria, 1955, pp. 245–253.

[6] R. Jaffee, C. Sims, J. Harwood, in: Proc. 3rd Plansee Seminar, Reutte, Austria, 1958, pp. 380–411.

[7] D. M. Mattox, Handbook of Physical Vapor Deposition (PVD) Processing, 2nd Edition, William Andrew Publishing, Oxford, UK, 2010.

[8] R. A. Powell, S. M. Rossnagel, A. Ulman, PVD for Microelectronics: Sputter Deposition Applied to Semiconductor Manufacturing Vol. 26, Academic Press, San Diego, USA, 1998.

[9] J. A. Thornton, J. E. Greene, in: R. F. Bunshah (Ed.), Handbook of Deposition Technologies for Films and Coatings, 2nd Edition, Noyes Publications, New Jersey, USA, 1994, pp. 275–345.

[10] D. Depla, S. Mahieu, J. E. Greene, in: P. M. Martin (Ed.), Handbook of Deposition Technologies for Films and Coatings, 3rd Edition, William Andrew Publishing, Oxford, UK, 2010, pp. 253–296.

[11] P. H. Mayrhofer, Materials science aspects of nanocrystalline PVD hard coatings, Ph.D. thesis, Montanuniversität Leoben, Austria (2001).

[12] P. Kelly, R. Arnell, Vacuum 56 (3) (2000) 159–172.

[13] U. of Kaiserslautern. Molecular beam epitaxy, http://www.physik.uni-kl.de/en/hillebrands/research/methods/molecular-beam-epitaxy/ [online, cited July 2016].

[14] M. Ohring, Material Science of Thin Films, Academic Press, San Diego, USA, 2001.

[15] C. A. Bishop, Vacuum Deposition onto Webs, Films and Foils, William Andrew Publishing, Oxford, UK, 2011, pp. 215–238.

[16] B. A. Movchan, A. V. Demchishin, Physics of Metals and Metallography 28 (4) (1969) 83–90.

[17] J. A. Thornton, Journal of Vacuum Science and Technology 11 (4) (1974) 666–670.

[18] R. Messier, A. P. Giri, R. A. Roy, Journal of Vacuum Science and Technology A 2 (2) (1984) 500–503.

[19] Y. Leterrier, Fragmentation Test Method for Adhesion Analysis of Coatings In Situ in a Microscope, Linkam Scientific, TST350 Application Notes, (2009).

[20] T. Li, Z. Suo, International Journal of Solids and Structures 44 (6) (2007) 1696–1705.

[21] N. Lu, Mechanics of hard films on soft substrates, Ph.D. thesis, Harvard University, USA (2009).

[22] A. Taylor, M. Cordill, L. Bowles, J. Schalko, G. Dehm, Thin Solid Films 531 (2013) 354 –361.

[23] C. Xie, W. Tong, Acta Materialia 53 (2005) 477–485.

[24] A. A. Taylor, M. J. Cordill, G. Dehm, Philosophical Magazine 92 (25-27) (2012) 3363–3380.

[25] T. Li, Z. Y. Huang, Z. C. Xi, S. P. Lacour, S. Wagner, Z. Suo, Mechanics of Materials 37 (2-3) (2005) 261–273.

[26] C. A. Bishop, Vacuum Deposition onto Webs, Films and Foils, William Andrew Publishing, Oxford, UK, 2011, pp. 177–185.

[27] M. Cordill, F. Fischer, F. Rammerstorfer, G. Dehm, Acta Materialia 58 (16) (2010) 5520–5531.

[28] Y. Leterrier, C. Fischer, L. Médico, F. Demarco, J.-A. E. Månson, P. C. P. Bouten, J. de Goede, G. Nisato, J. A. Nairn, in: Proc. 46th SVC Annual Technical Conference, Society of Vacuum Coaters, San Francisco, USA, 2003, pp. 169–175.

[29] R. D. Bland, G. J. Kominiak, D. M. Mattox, Journal of Vacuum Science and Technology 11 (4) (1974) 671–674.

[30] A. F. Mayadas, M. Shatzkes, Physical Review B 1 (1970) 1382–1389.

[31] O. Glushko, M. Cordill, Experimental Techniques (2014) 1–8.

[32] N. C. Woo, K. Cherenack, G. Tröster, R. Spolenak, Applied Physics A 100 (1) (2010) 281–285.

[33] O. Glushko, V. Marx, C. Kirchlechner, I. Zizak, M. Cordill, Thin Solid Films 552 (2014) 141 – 145.

[34] G. Leichtfried, J. H. Schneibel, M. Heilmaier, Metallurgical and Materials Transactions A 37 (10) (2006) 2955–2961.

[35] H. Okamoto, Journal of Phase Equilibria and Diffusion 31 (6) (2010) 580–581.

[36] Y. N. Gornostyrev, M. I. Katsnelson, G. V. Peschanskikh, A. V. Trefilov, Physica Status Solidi (b) 164 (1) (1991) 185–193.

[37] N. I. Medvedeva, Y. N. Gornostyrev, A. J. Freeman, Physical Review B 72 (2005) 134107.

[38] N. Medvedeva, Y. Gornostyrev, A. Freeman, Acta Materialia 50 (10) (2002) 2471–2476.

[39] G. Gottstein, Physikalische Grundlagen der Materialkunde, Springer, Berlin Heidelberg, Germany, 2001, in German.

[40] J. Chan, P. Friedberg, Four-Point Probe Manual, The University of California, Berkeley, USA (2002).

[41] G. Norberg, S. Dejanovic, H. Hesselbom, IEEE Transactions on Components and Packaging Technologies 29 (2) (2006) 371–378.

[42] M. D. Abràmoff, P. J. Magalhães, S. J. Ram, Biophotonics International 11 (7) (2004) 36–42.

[43] M. Cordill, V. Marx, in: MRS Proceedings, Vol. 1527, DOI: 10.1557/opl.2013.617, 2013.

[44] Reference patterns of Mo (ICDD 03-065-7442), Mo_3Re (ICDD 01-071-9799) and Re (ICDD 01-071-6589) from the database of the International Centre for Diffraction Data, ICDD PDF-2 Release 2007.

[45] V. S. Postnikov, V. V. Postnikov, V. S. Zheleznyi, Physica Status Solidi (a) 39 (1) (1977) 21–23.

[46] J. R. Gavaler, M. A. Janocko, C. K. Jones, Applied Physics Letters 21 (1972) 179–180.

[47] S. Rosen, J. Goebel, J. Mullins, Journal of the Less Common Metals 12 (6) (1967) 510–512.

[48] E. Ivers-Tiffée, W. von Münch, Teubner, Wiesbaden, 2007, in German.

[49] A. Hofer, J. Schlacher, J. Keckes, J. Winkler, C. Mitterer, Vacuum 99 (2014) 149–152.

[50] R. Hummel, Electronic Properties of Materials, Springer, New York, USA, 2011.

[51] R. Powell, R. Tye, M. J. Woodman, Journal of the Less Common Metals 5 (1) (1963) 49–56.

[52] H. Köstenbauer, G. A. Fontalvo, M. Kapp, J. Keckes, C. Mitterer, Surface and Coatings Technology 201 (8) (2007) 4777–4780.